MTLA 35 (2024) 102127

Contents lists available at ScienceDirect

Materialia

journal homepage: www.elsevier.com/locate/mtla

Full Length Article

Effect of combined additions of Sc, Zr and Ti on hot-cracking resistance and precipitation behaviour in Al-Mg alloy by L-PBF

F. Larini [a,*], R. Casati [a], S. Marola [a], C. Andrianopoli [b], P. Bajaj [b], M. Vedani [a]

[a] Department of Mechanical Engineering, Politecnico di Milano, Via G. La Masa 1, 20156 Milano, Italy
[b] m4p material solutions GmbH - Gewerbestraße 4, 9181 Feistritz im Rosental, Austria

ARTICLE INFO

Keywords:
Additive manufacturing
Laser powder bed fusion
High-strength Al alloys
Microstructure
Heat treatment
precipitation behaviour

ABSTRACT

The request for high-performance aluminum components prompts research into innovative alloys compatible with laser-based additive manufacturing processes, leveraging grain refiners in their composition to mitigate hot-cracking and enhance strength. While the addition of Sc and Zr in Al-Mg alloys has been widely investigated, the high cost and supply risks associated with Sc necessitate reducing its amount and replacing, at least partially, with other inoculants. In this preliminary study, the amount of Sc replaceable with different concentrations of Zr or Ti is evaluated investigating the laser powder bed fusion processability of three powder feedstocks: a pre-alloyed Al-Mg-Zr-Sc powder, a blend of the previous alloy with addition of Zr particles, and a further blend of an alloy depleted of Zr with added Ti particles. The experimental analyses on the laser-processed alloys showed that the standard and the Zr-enriched alloys featured a bimodal microstructure free from cracks with fine equiaxed grains at the edge of the molten pools and coarser grains at their centers. In the alloy variant depleted in Zr with addition of Ti particles a columnar structure was observed and hot-cracks appeared. Thermodynamic simulations of phase formation allowed defining the precipitation kinetics during solidification and direct aging, showing increased precipitation in alloys with higher Zr content, while the presence of Ti resulted in sluggish precipitation. Experimental aging tests demonstrated significant increases in microhardness, with peak values of the modified alloys achieved after 12 h at 375 °C.

1. Introduction

Additive manufacturing, or 3D printing, has revolutionized the industrial landscape by introducing new possibilities in the production of complex components. Among the many available techniques, laser powder bed fusion (PBF-LB/M) emerges as a cutting-edge methodology that has profoundly influenced industrial additive manufacturing [1]. This technology is based on the principle of depositing thin layers of metal powder and subsequently melting in a layer-by-layer fashion selected areas of the powder bed using a laser beam, creating a three-dimensional object according to a Computer-Aided Design (CAD) model [2].

Powders are a fundamentally important element of the printing process, as they strongly influence the quality of the final component and the content of defects. It is known that many commercial powders are manufactured by atomization starting from pre-alloyed raw materials (e.g. electrodes, ingots), which ensure the uniform distribution of all elements in each powder particle, guaranteeing uniform batches, greater control during printing, and a homogeneous printed part [3–6]. On the other hand, the atomization process to obtain pre-alloyed powder is an expensive and time-consuming process, not very suitable for modifying current alloys and performing initial tests on small quantities of powder. To investigate novel PBF-LB/M alloys, faster and cheaper alternatives are evaluated, especially for the preliminary screening phases [7]. Vieth et al. proposed a strategy based on the ultrasonication wet coating of Al7075 with TiC nanoparticles. Despite the effectiveness of the method, the main critical issues concern the potential formation of agglomerates in the aqueous solution, and the drying of powders with the risk of oxidation and contamination of the alloy [8]. Ball milling is an alternative method to join particulate materials on the base powder surface. This process has the advantage of dry coating via mechanical interlocking but severely deforms the shape of the powder particles, deviating from the optimal spherical condition and affecting flowability [9]. The cheapest method that keeps the morphology of the powders unchanged is mechanical mixing [10]. This approach is highly used in the research of novel alloys because it is easily accessible, enables the

* Corresponding author.
E-mail address: federico.larini@polimi.it (F. Larini).

https://doi.org/10.1016/j.mtla.2024.102127
Received 22 March 2024; Accepted 15 May 2024
Available online 16 May 2024

investigation of many different compositions starting from batches of standard powders or pure elemental powders, and maintains a high flowability. The main drawback lies in the lower repeatability of the batches and risk of segregations, leading to different printed parts and non-homogeneous chemical-physical properties and microstructure. Although it is not the most used technique for commercial powders, it is worth mentioning that there exist blended powders available on the market for popular high-strength alloys [11–13].

Among metallic materials, aluminum alloy have quickly attracted the attention of researchers and designers of lightweight parts to be produced by AM routes. The choice of aluminum in PBF-LB/M technology is motivated by its high thermal and electrical conductivity, corrosion resistance, and low density, crucial factors in applications where weight and thermal performance are critical. However, the range of aluminum alloys available on the market is still very limited, due to the challenges related to the production process [14]. Indeed, the high thermal conductivity of aluminum can cause rapid heat dissipation, and the high cooling rates during solidification causes internal stresses and the appearance of unwanted hot-cracks in the most critical alloys [15]. To prevent the problem of these defects, typically encountered in high-strength alloys, the most validated approach is the use of inoculants, nanometric particles that act as nucleation sites, promoting the generation of finer and equiaxed grains upon solidification, thus reducing the formation of hot-cracks. The effectiveness of inoculants largely depends on their crystallographic structure. The main requirement is the formation of particles having coherent or semi-coherent interfaces with the Al matrix to reduce interfacial energy, thus favouring the heterogeneous nucleation of α-Al grains from the melt. The most used strategies are the use of ceramic particles (for example TiB_2, TiC, and SiC) or intermetallic compounds [16–18]. In particular, in aluminum alloys the addition of elements such as Sc, Zr or Ti has proven effective in creating primary Al_3M particles (where M represents one or a combination of the above elements), which promote columnar to equiaxed grain transition (CET) [18–20]. Fine grains lead to a better redistribution of the liquid film in the last stages of solidification and limits the formation of long interdendritic channels, thus preventing the initiation and growth of hot-cracks.

Croteau et al. have successfully printed two pre-alloyed Al-Mg-Zr alloys confirming that cubic nanosized $L1_2$ Al_3Zr which solidify at high temperature, allow the heterogeneous nucleation of aluminum grains. In addition, further strengthening Al_3Zr precipitate could form during the subsequent aging of the alloy, starting from a Zr supersaturated solid solution [21]. The effects of transition elements (Ti, Zr) and rare earths (Sc) on the grain refinement of aluminum have been comprehensively explained by Lei et al. [22]. In aluminum alloys, when the Sc and Zr contents are lower than the eutectic or peritectic point (0.55 wt.% for Sc and 0.1 wt.% for Zr, respectively), the elements exist in the solute form and their segregation at the solid-liquid interface during crystallization promote the undercooling responsible for the refinement of the α-Al matrix. Beyond the eutectic or peritectic composition, Al_3Sc and Al_3Zr start to be the main phases containing Sc and Zr, and the refinement mechanism becomes more effective thanks to the heterogeneous nucleation mechanism. The excess Sc and Zr entrapped in solid solution after rapid solidification, additionally plays a key role in increasing the mechanical properties of the alloy owing to aging, which causes the precipitation of secondary $Al_3(Sc,Zr)$ phases. Spierings et al. studied the effect of different heat treatments on the commercial pre-alloyed Scalmalloy® (Al-4.4Mg-0.8Sc-0.3Zr-0.5Mn) and obtained that after 4 h of soaking at 350 °C the alloy preserved its as-built bimodal microstructure – characterized by fine grains at the boundary and coarse grains at the center of the melt pools – and achieved an ultimate tensile strength (UTS) of 515 MPa and a yield strength (YS) of 450 MPa [23]. Instead, the addition of Ti as the main element of Scantital® (Al-1Ti-1Sc-0.4Zr) generates an equiaxed ultrafine microstructure across various weld tracks, thanks to the formation of numerous primary Al_3Ti and $Al_3(Sc,Zr,Ti)$ precipitates [24]. The addition of elements such as Sc and Zr is believed to produce a synergistic effect in the formation of tri-aluminide intermetallics. This justifies the combined use in the pre-alloyed StrengthAl (Al-5.2Mg-0.8Zr-0.3Sc), a commercial alloy that exploits Zr and Sc to refine the grain, avoid hot-cracking phenomena and strengthen by aging the printed part [25]. Finally, it is worth pointing out that in the latest report of 2023, the European Commission confirmed Sc as a Critical Raw Materials (CRM) [26], i.e. an element with both a high economic importance and a high supply risk for the EU. On the contrary, Zr and Ti are not included in the CRMs list, suggesting the opportunity of replacing at least partially Sc with these latter elements in high-strength Al alloys.

The main objective of this work is to preliminarily evaluate the extent of Sc replaceable by varying concentrations of Zr and Ti, while maintaining high-strength Al alloys characteristics suitable for processing via PBF-LB/M. In a first phase, novel alloys were created by mechanically mixing a pre-alloyed commercial Al-Mg-Zr-Sc powder with Zr particles or Ti particles. In particular, the commercial m4p™ StrengthAl was used as the pre-alloyed reference material, while two modified alloys were obtained as a mixture of StrengthAl with the addition of Zr particles, and as a variant of StrengthAl with reduced content of Zr and addition of Ti. With this approach, supported by Calphad-based simulations, it was possible to investigate not only the processability and performance of the novel alloys compared to the reference alloy, but also to evaluate the effects of compositional heterogeneities due to elemental powder mixing.

2. Materials and methods

The three powder feedstocks were supplied by m4p material Solution GmbH: a pre-alloyed Al-Mg-Zr-Sc powder commercially available as m4p™ StrengthAl (S); a blend obtained by mechanically mixing the StrengthAl powder and Zr particles (*S*+Zr); a blend of a variant of the StrengthAl powder depleted in Zr with added Ti particles (S-Zr+Ti). The geometrical features of the powders were investigated through a Malvern Morphologi 4 automatic imaging microscope. A minimum of 34,000 particles were analyzed to statistically measure the geometric characteristics of each powder feedstock. The Circular Equivalent (CE) Diameter was considered for the evaluation of the particle size distribution (PSD).

A Renishaw AM 250 PBF-LB/M system equipped with a reduced built volume (RBV) device was used to produce sets of $10\times10\times15$ mm^3 samples, which were printed directly on a non-preheated Al platform without any support structure. To reduce oxygen contamination, Ar gas was flown inside the build chamber during the process. The following parameters were set for each print, after optimization: laser power 200 W, layer thickness 25 μm, laser hatch distance 120 μm, laser exposure time 140 μs and point distance 40 μm, corresponding to a volumetric energy density (VED) [27] of 233 J/mm^3. A scanning strategy consisting of parallel laser track lines was used. Laser direction was rotated of 67° after each layer completion. The relative density of the samples was measured by image analysis. In particular, three light optical microscope (LOM) images at 2.5X magnification were taken on the vertical section of the samples. Each image was subsequently analyzed using ImageJ software and the relative density was calculated as the ratio of pore area to total area examined. The relative density of the sample was calculated as the average value of the relative densities measured for three sections.

The chemical composition of the as-built samples printed with optimized parameters was measured by a Bruker Q4 Tasman spark-Optical Emission Spectrometer (OES). Due to the unavailability of calibration standards for Zr and Sc, the concentration of these elements was measured by Energy Dispersive Spectrometry (EDS).

The evaluation of the potential strengthening ability of the alloys and the preliminary design of the heat treatments was simulated with the Thermo-Calc® software (using the TCAL8 v8.2 database for Al alloys and MOBAL7 v7.0 database for Al-Alloys Mobility). The precipitation of strengthening tri-aluminide intermetallics during direct aging was

studied considering the bulk α-Al matrix as nucleation site, spherical morphology of the Al_3M precipitates and isothermal-type calculation. The computation, based on the Langer-Schwartz theory and the Kampmann-Wagner numerical approach [28], considers the quantity of Zr/Sc/Ti remaining in solid solution at the completion of solidification, thus not participating in the formation of primary grain refiner precipitates. The simulations were run for the S, S+Zr, and S-Zr+Ti alloys, setting four different soaking temperatures, namely 300, 350, 400 and 450 °C.

The actual aging response of the alloys was then investigated on $10\times10\times5$ mm^3 samples, printed with optimized process parameters and directly aged in a muffle furnace in air for different times (1, 2, 4, 8, 12, 24 h) at 350, 375, 400 °C, and subsequently water quenched. On the square face of the samples, Vickers microhardness tests were performed with a load of 500 g and a dwell time of 15 s. For each condition, the resulting microhardness value was the average of five measurements taken on samples previously ground down to 2500 grit paper.

Ground and polished samples with a 50 nm colloidal silica solution were used for metallographic analyses at the Nikon Eclipse LV150NL light optical microscope (LOM) and Zeiss Sigma 500 Field Emission Scanning Electron Microscope (FE-SEM) equipped with the Oxford Instruments Ultim Max EDS detector and electron backscattered diffraction (EBSD) detector mod. Oxford Instruments C—Nano. Chemical etching of samples, when required, was performed using the Keller's reagent, diluted with 80 % distilled H_2O.

3. Results and discussion

3.1. Powder characterization

Fig. 1a shows the PSD measured for the three powder feedstocks of the S, S+Zr, and S-Zr+Ti alloys. Two peaks are observed in the standard alloy S. The main peak is between 20 and 80 μm, indicating that most of the particles fall within this range. A low intensity secondary peak, related to the presence of satellites, is centered around 7 μm. The curves relating to the two powder blends are easily recognizable due to a marked bimodal distribution in which the main peak of S particles is unchanged in position, while the intense secondary peaks, shifted towards values of around 1–2 μm, are assumed to be caused by the contribution of the added Zr or Ti particles and the presence of satellites detached from the S powder during the mechanical mixing phase. In fact, from SEM investigations the minimum size of the added traced particles is around 3 μm, while their maximum size is 30 μm (Fig. 1c-d). The added particles appear brighter than the S alloy, due to the higher atomic number of Zr and Ti (40 and 22, respectively) compared to Al (13) which produces a less intense backscattered electron signal. As shown by the quantitative data summarized in Table 1, the S alloy features a D10 value of 9.64 μm, while the S+Zr and S-Zr+Ti alloys have 1.68 and 1.78 μm, respectively. Considering D90, all the investigated feedstocks are similar, showing values ranging from 45.7 to 49.2 μm.

3.2. As-built microstructure

The chemical composition of the as-built samples is reported in Table 2.

Samples printed with optimized process parameters revealed a maximum relative density of 98.9 %, 99.1 %, and 99.2 % for the S, S+Zr, and S-Zr+Ti alloy, respectively.

The as-built samples were etched to highlight the laser tracks and evaluate the grain size on sections perpendicular to the build platform.

Table 1
Powder particle size (D10, D50, D90, and span) of the three powder feedstocks.

Alloy	D10 [μm]	D50 [μm]	D90 [μm]	Span (D90-D10)/D50
S	9.64	33.18	49.21	1.19
S+Zr	1.68	25.18	45.71	1.75
S-Zr+Ti	1.78	25.11	47.60	1.82

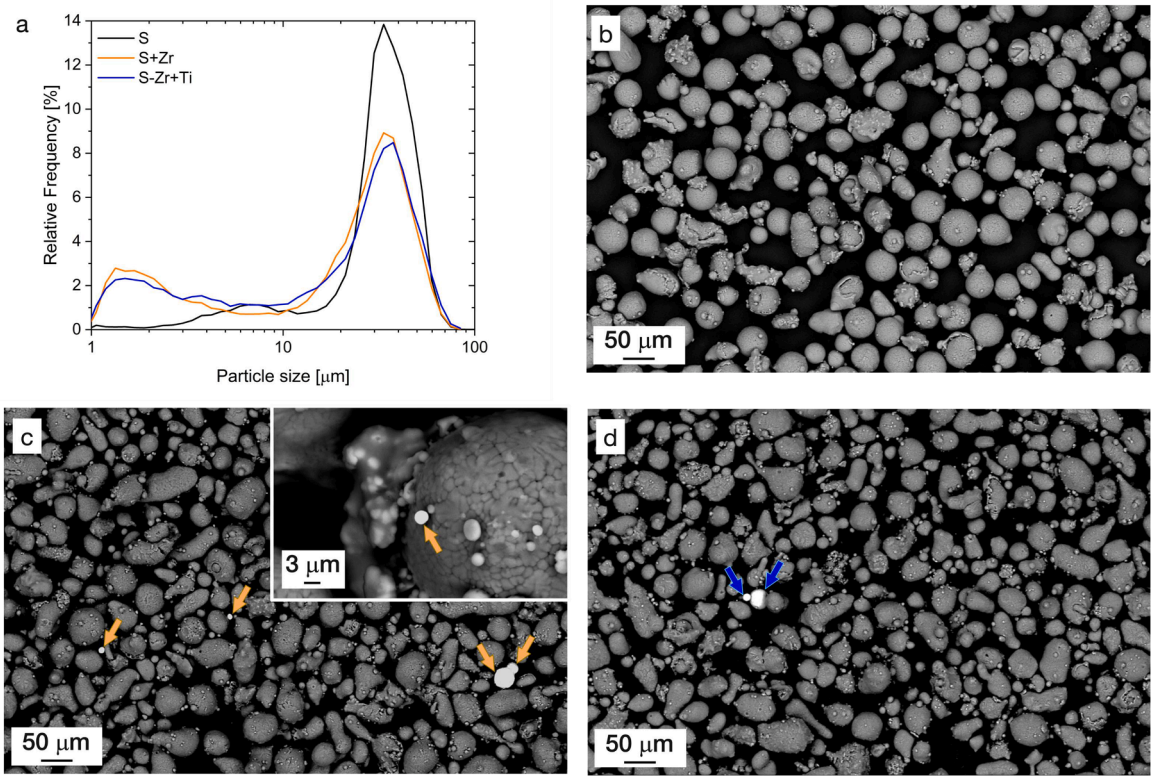

Fig. 1. Analysis of the powder feedstocks through particle size distribution curves (a) and morphology investigations. S alloy (b), S+Zr alloy (c), and S-Zr+Ti alloy (d). The orange and blue arrows show the Zr and Ti particles, respectively.

Table 2
Chemical composition (in wt.%) of as-built S, *S*+Zr, and S-Zr+Ti alloy samples.

Alloy	Mg	Zr	Sc	Ti	Fe	Al
S	4.5 ± 0.2	0.79 ± 0.03	0.32 ± 0.01	–	0.082 ± 0.002	bal.
S+Zr	3.9 ± 0.1	0.89 ± 0.15	0.31 ± 0.03	–	0.059 ± 0.002	bal.
S-Zr+Ti	4.0 ± 0.4	0.34 ± 0.06	0.34 ± 0.03	0.20 ± 0.06	0.27 ± 0.13	bal.

At low magnifications, the typical fish-scale morphology resulting from repeated laser scans can be appreciated (Fig. 2). On the investigated sections, limited gas porosity with a diameter of few microns is found, and no cracks are present. At higher magnifications, the distribution of cuboidal nano-precipitates mainly concentrated at the edges of the molten pools can be observed. These bright particles are mainly located within the fine equiaxed grains with diameter of about 1 μm. Given the high Zr and Sc content detected by EDS analysis and the characteristic cubic shape, it is assumed that they are the primary precipitates of Al_3(Sc,Zr), responsible for the grain refinement [21].

The EBSD analysis results are displayed in Fig. 3. The S sample (Fig. 3a) shows a strong bimodal grain structure, with alternating fine equiaxed grains at the edges of the melt pools and coarser grains at their centers, which sometimes tend to a columnar configuration. This microstructure has extensive evidence in the literature [21,24,29]. According to Belelli et al., the Al_3Zr and Al_3Sc phases in StrengthAl alloy start to precipitate at 910 °C and 684 °C, respectively, above the onset of solidification of the α-Al matrix [25]. Although it is known that the fine-grained regime is closely associated with the formation of nano-precipitates that act as nucleation sites for new grains, their non-homogeneous distribution in the melt pool is still under investigation. According to Griffiths at al. the distribution of the precipitates could be explained by the change of the solidification front velocity in the different regions of the melt pool [30]. In particular, the inoculants would precipitate at the edge of the molten pool due to the low speed of the solidification front, while its increase in the center of the pool would lead to a suppression of the nucleating effect and an increase in solute trapping. Another study assumes that the edge of the molten pool cools down more rapidly due to direct contact with the already solidified underlying layer, which acts as a heat sink for the molten material. Consequently, the rapid cooling favors the formation of smaller grains along the edge of the laser tracks, which nucleate from the Al_3(Sc,Zr) nanoparticles dispersed in the liquid [29]. Finally, convective currents in the molten material could contribute to an inhomogeneous distribution and the segregation of the first precipitates floating in the liquid, while the slower cooling at the center of the molten pool supposedly combined with the absence of nano-nucleants leads to the formation of larger grains that nucleate epitaxially from the solidified edge and grow competitively along the direction of the thermal gradient [31]. This microstructural non-uniformity can be mitigated through multiple scans that remelt the columnar grain region and form equiaxed grains starting from the original scan [30].

The addition of 0.1 wt.% Zr particles blended to the standard alloy has two main effects on the as-built microstructure (Fig. 3c-d). First, the bimodal structure in the S+Zr alloy is characterized by a clear grain refinement with respect to S alloy (1.92 μm^2 and 4.11 μm^2, respectively). It is observed that the fine grains located at the edges of the molten pools are approximately the same size in both alloys, but they extend over a larger distance toward the centre in the S+Zr alloy. About 45 % of the grains in the S+Zr have an area below 1 μm^2, compared to about 20 % in the S alloy. Consequently, the coarse-grain area corresponding to the center of the molten pools has a smaller extension and the coarsening of the grains is reduced. Secondly, the chemical inhomogeneity of the powder feedstock is partially reflected in the as-built part. In fact, the SEM images of the S+Zr sample highlight areas with different brightness (Fig. 3c, SEM image), corresponding to zones enriched with variable amounts of Zr.

Moreover, as shown in Fig. 4a, it was noticed that some large-diameter Zr particles coud only partially melt during the printing process (the melting point of pure Zr is 1855 °C), resulting in bright striations, star-shaped Zr-based clusters, and coarse residuals of the partially melted particles larger than 10 μm. Fig. 4b reports the EBSD image of the same area depicted in Fig. 4a. The partially melted Zr could not be distinguished from the α-Al matrix during EBSD indexing, but it is apparent that the presence of the coarse Zr particles does not affect the grain refinement action. Despite the heterogeneous distribution of the residual Zr particles, the grains are refined on a local scale and their bimodal size distribution is assumed to be mainly governed by the local solidification rate, as described above. The overall higher quantity of Zr leads to a general refinement, while the presence of residues of the Zr particles does not seem to alter the adjacent structure.

Finally, the S-Zr+Ti alloy sample showed the presence of small-size hot-cracks spread along the entire sample (Fig. 3e). The EBSD results clearly show the development of large columnar grains through multiple melt pools, with an increase in the average grain area (11.97 μm^2) and the presence of grains exceeding 110 μm^2 (Fig. 3f). For this alloy, it can be stated that the reduced presence of refining elements was not able to form enough Al_3M nano-nucleants to prevent the columnar growth of grains.

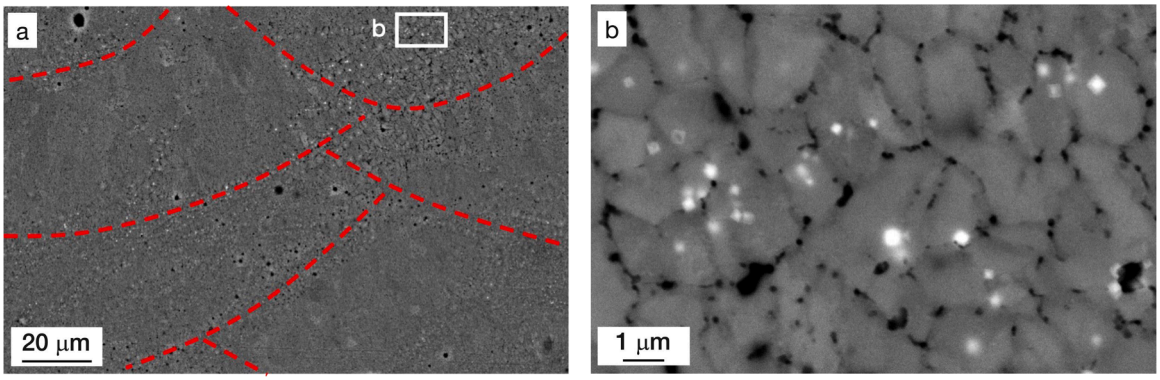

Fig. 2. FE-SEM images at low (a) and high (b) magnification collected on vertical section of as-built S sample.

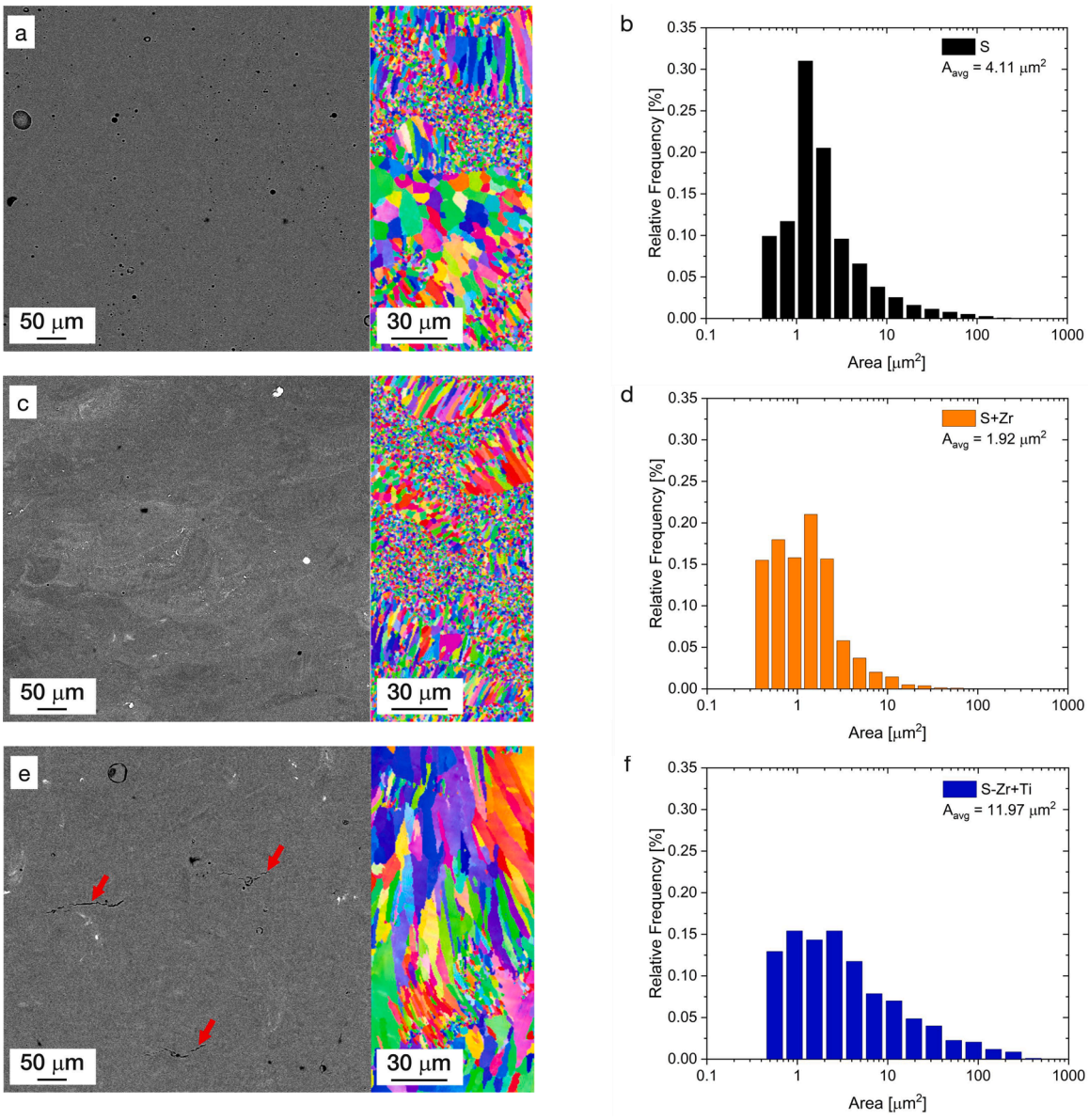

Fig. 3. SEM images, EBSD inverse pole figures, and relative frequency of grain size area in S (a-b), S+Zr (c-d), and S-Zr+Ti (e-f) samples. The red arrows show the presence of hot-cracks.

3.3. Simulation of aging behavior

For each alloy, the precipitation kinetics of the Al_3M particles was calculated using the Thermo-Calc® software, employing the TCAL8 v8.2 and MOBAL7 v7.0 databases. The isothermal computation was set up considering a spherical morphology of the reinforcing tri-aluminides, nucleating within the bulk of the material. Fig. 5a-c shows simulations of the precipitation kinetics through the trends of mean radius (MR), number density (ND) and volume fraction (VF) of the precipitated particles considering 4 direct aging temperatures, namely 300, 350, 400, and 450 °C. The volume fraction is related to the mean radius and number density according to the following relationship:

$$VF = \frac{4}{3}\pi(MR)^3 \cdot ND$$

From the observation of the mean radius curves, it is apparent that the three alloys show a substantially similar behavior (Fig. 5a). At each temperature, an initial nucleation phase in which the particle size remains almost constant is followed by a growth phase characterized by an exponential increase of the mean radius with soaking time. The increase of aging temperature accelerates the kinetics of the process, leading to anticipated nucleation and growth. For example, at 300 °C the Al_3M particles start to precipitate after 10 h, while at 450 °C nucleation is expected to start in a few seconds.

The volume fraction is characterized by an S-curve that rises quickly, and subsequently stabilizes at the maximum value (Fig. 5b). Higher temperatures lead to the dual effect of shorter nucleation times and smoother trend to the maximum plateau value. This phenomenon is particularly evident for the S-Zr+Ti alloy, where the presence of Ti seems to modify the precipitation kinetics compared to the S and S+Zr alloys. In fact, the latter share the same S-curve shape, with relatively short time to reach the plateau and maximum S+Zr values slightly higher than S alloy (0.018 and 0.017, respectively) due to the higher Zr content. In contrast, the S-Zr+Ti alloy is characterized by a similar rapid growth up to approximately 0.008, but this is followed by a more sluggish growth up to the plateau, at approximately 0.015. At each temperature, there is a clear difference in the time required to achieve the maximum volume fraction. For example, considering the curves at

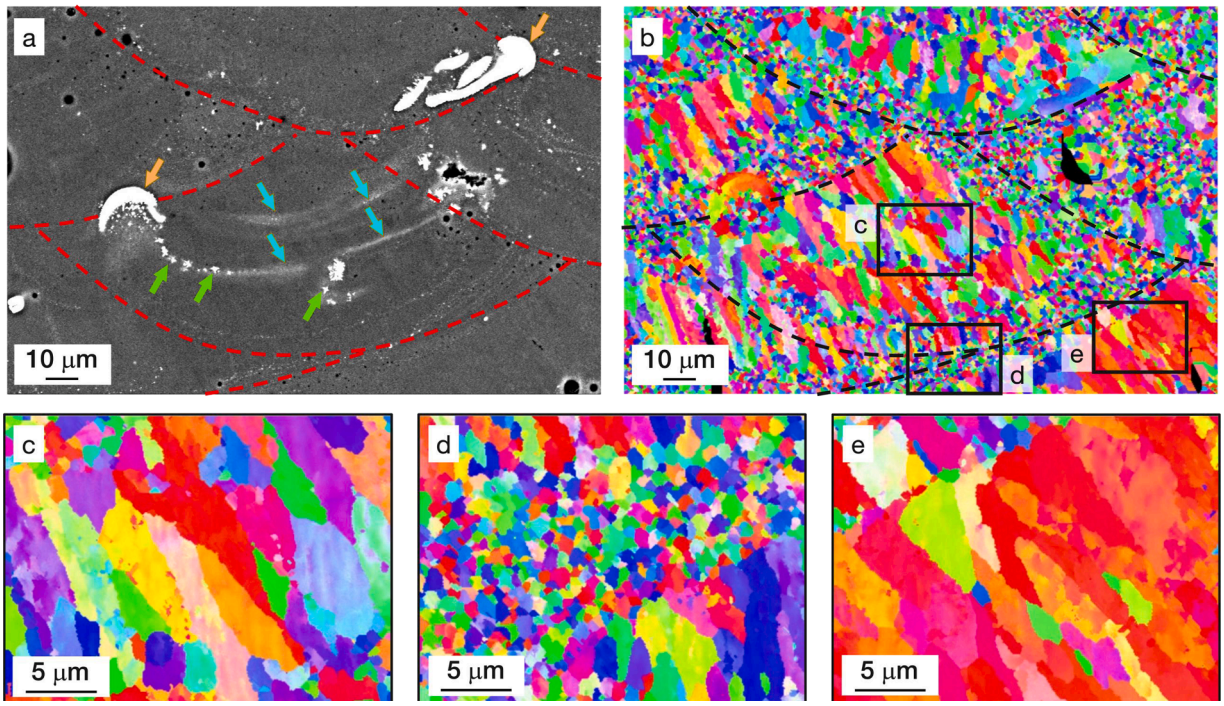

Fig. 4. SEM image (a) and corresponding EBSD inverse pole figure (b) of a melt pool in the as-built vertical section of a S+Zr sample. The dashed red and black lines indicate the melt pool boundaries. The orange, green, and light blue arrows show partially melted Zr particles, star-shaped Zr-based clusters, and bright striations, respectively. Higher magnification EBSD images of the highlighted areas in figure (b) are displayed in figures (c) to (e).

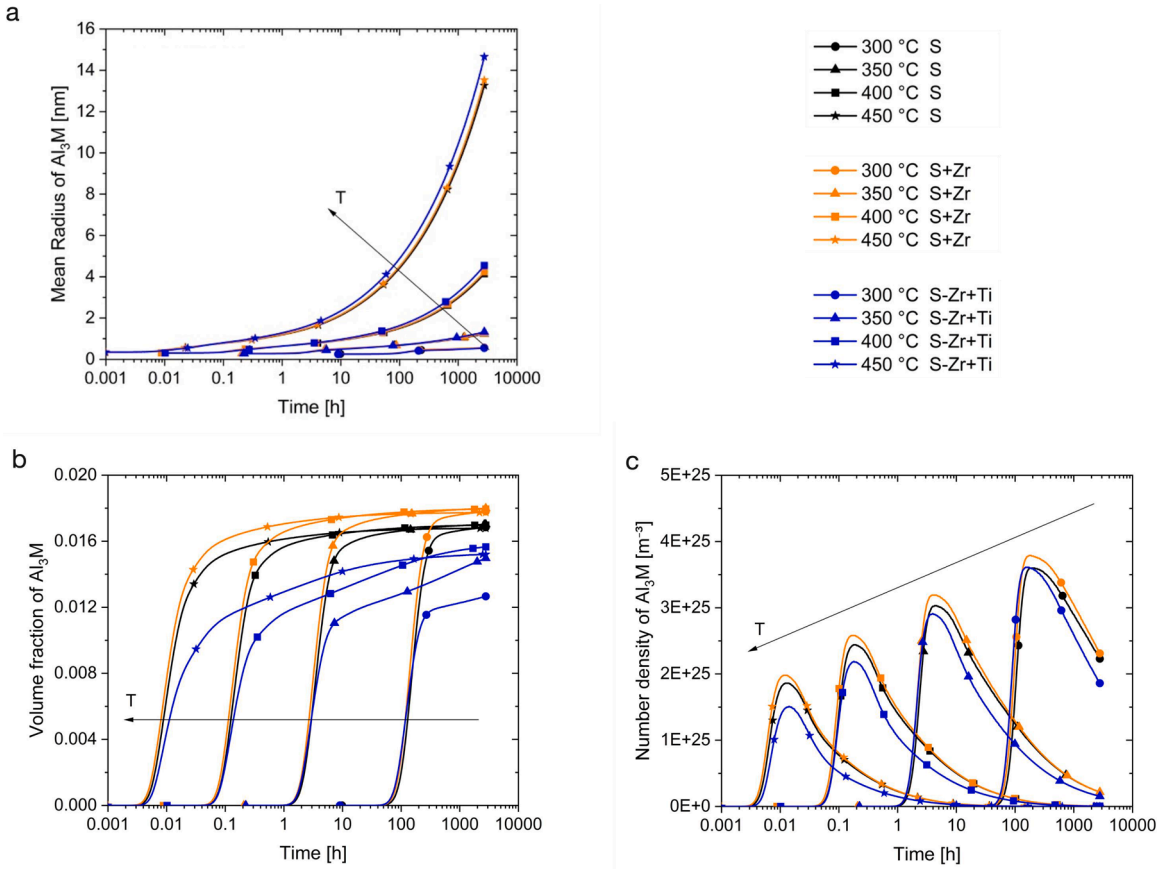

Fig. 5. Simulation of Al_3M precipitation in bulk S, S+Zr, and S-Zr+Ti alloys, considering mean radius (a), volume fraction (b), and number density (c) of particles.

450 °C, the S and S+Zr alloys reach the maximum value after 1 h, while the S-Zr+Ti requires a period 100 times longer. As reported in numerous studies, Zr and Sc are extremely effective in the formation of Al_3M precipitates from the decomposition of the supersaturated solid solution, and their synergistic effect is exploited to strengthen the matrix [22,32]. In particular, despite the higher content of Zr compared to Sc, direct aging simulations on StrengthAl carried out in another study did not predict the formation of secondary Al_3Zr precipitates but only $Al_3(Sc,Zr)$ precipitates in which the volumetric fraction of the transition elements decreased proceeding from the core to the edge of the cell, according to a concentration gradient [25]. The role of Ti was addressed by Knipling et al., who considered the nucleation and precipitation strengthening in Al-0.2Zr and Al-0.2Ti (at.%) alloys [33]. According to this study, Ti is added in Al alloys mainly to refine the grain structure, while Zr is added for its greater effectiveness in forming coherent dispersoids precipitated from supersaturated solid solution. Indeed, Al_3Zr secondary phases are more readily precipitated during higher temperature aging than Al_3Ti. The volume fraction curves of S-Zr+Ti could therefore be characterized by the initial rapid growth provided by the precipitation of $Al_3(Sc,Zr)$, while it can be assumed that Ti subsequently intervenes causing a further sluggish precipitation. The effect of the direct aging temperatures can be deduced from the diagram in Fig. 5b. It can be observed that the aging curve at 300 °C cannot lead to the maximum expected precipitation in reasonable times, suggesting the selection of higher temperatures (at least 350 °C) for the experimental tests.

Finally, Fig. 5c shows the curves related to the number density of Al_3M precipitates at different aging temperatures. The bell-shaped trend highlights three steps: (i) nucleation and growth of Al_3M precipitates in the rising portion of the curves; (ii) maximum number of particles achieved at the apex of the curve; (iii) coarsening of particles, also confirmed by the concurrent constant volume fraction and increase in mean radius (Fig. 5a-c). The increase in temperature has the general effect of anticipating and lowering the number density curves. Finally, it can be considered that the overall strengthening effect promoted by the precipitated particles can be assessed by well-established theories stating that the potential strengthening is directly proportional to the square root of the volume fraction of precipitates and inversely proportional to its size [34]. Fig. 6 shows the expected trend for this combined parameter at 350 and 400 °C in order to assess the effectiveness of the strengthening as a function of aging time.

3.4. Evolution of hardness upon aging

Experimental aging tests were performed on the three aluminum alloys to monitor the evolution of microhardness as a function of time.

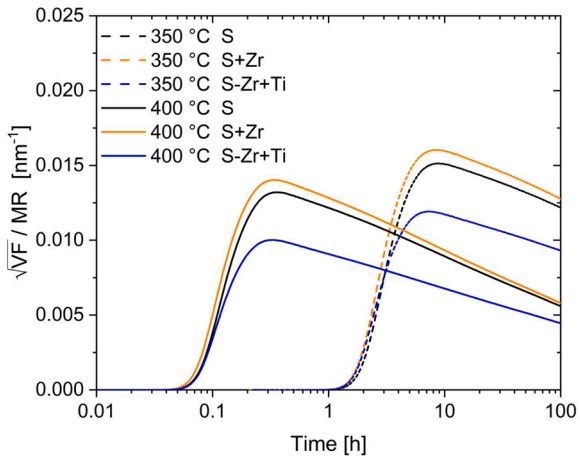

Fig. 6. Evaluation of the dispersion strengthening through the relationship between mean radius and volume fraction of Al_3M precipitates [34].

Direct aging at 350, 375 and 400 °C were selected. Based on Thermo-Calc® simulations, at these temperatures, the precipitation of Al_3M particles occurs in reasonable aging times. Six soaking times were investigated, namely 1, 2, 4, 8, 12, and 24 h. As depicted in Fig. 7, the as-built microhardness of the S sample is 99.8 $HV_{0.5}$, a higher value compared to the S+Zr and S-Zr+Ti powder blends which attained 91.0 and 81.4 $HV_{0.5}$, respectively. In spite of the finer grain size achieved in the S+Zr alloy, the reduced hardness is likely attributed to its lower magnesium content (Table 2) that limits the solid solution strengthening effect [35].

In general, all the investigated temperatures were effective in rapidly strengthening the alloys. Indeed, after 1 h of aging, a minimum increase in hardness of 35 % is recorded for each condition. The S-Zr+Ti curves are constantly lower than those of the other investigated alloys, due to the lower content of alloy strengthening elements and the presence of hot-cracks which might have weaken the structure. Direct aging at 350 °C leads to a slow but constant increase in microhardness (Fig. 7a). The maximum values are recorded after 24 h, but the trend of the curves suggests a drop in hardness at even longer times. Shifting to higher aging temperatures leads to shorter aging times. After 12 h at 375 °C, peaks at 147.2 and 137.8 $HV_{0.5}$ are recorded for the S+Zr and S-Zr+Ti alloys, respectively (Fig. 7b). Alloy S shows values in line with S+Zr alloy but a faster response to aging, reaching the peak after 2 h only. Finally, the treatment at 400 °C further accelerates the precipitation process and all alloys reach the maximum value within 2 h (Fig. 7c). These general results are in good qualitative agreement with the trend already presented in Fig. 6, derived from the reprocessing of Thermo-Calc® data. It can be observed that the calculated peak-aging times are slightly underestimated whereas the relative position of the three alloys is correctly captured.

Finally, it is worth considering that no significant differences have been detected when comparing the microstructures of as built and aged samples by FE-SEM, see for example Fig. 8 for the S alloy. Future investigations will be devoted to characterization of the precipitates formed during aging by TEM analyses.

4. Conclusion

The present study was aimed at assessing the opportunity of partially replacing Sc with Zr and Ti in an Al-Mg alloy targeting improved PBF-LB/M processability. In the presented first step of the research, novel alloys were created by mechanically mixing a pre-alloyed commercial Al-Mg-Zr-Sc powder with Zr particles and Ti particles to generate different amounts of nucleation agents and strengthening precipitates during solidification and aging, respectively.

The processing of the investigated alloys by Laser powder bed fusion and the study of their microstructure and precipitation behavior led to the following conclusions.

- The as-built reference pre-alloyed Al-Mg-Zr-Sc alloy featured a bimodal microstructure with fine equiaxed grains at the edges of the melt pools and coarser grains at their centers. Moderate addition of Zr refined grain size, while the replacement of part of the Zr with Ti revealed to be less efficient, showing a columnar grain structure and small hot-cracks. This suggests that the combination and amount of inoculating elements in this alloy was not sufficient to promote the columnar to equiaxed grain transition.
- The inhomogeneity of the powder feedstock affects on the local scale the elemental chemical distribution of the as-built microstructure of the modified alloys obtained by blending different powders. After Laser processing, traces of partially melted Zr and Ti particles were still observed in the microstructure.
- Thermo-Calc® simulations were employed to evaluate the Al3M precipitation kinetics during direct aging. Results showed that the alloy variant with the higher Zr content showed potential for increased Al3M-type precipitation. In the alloy containing Zr and Ti,

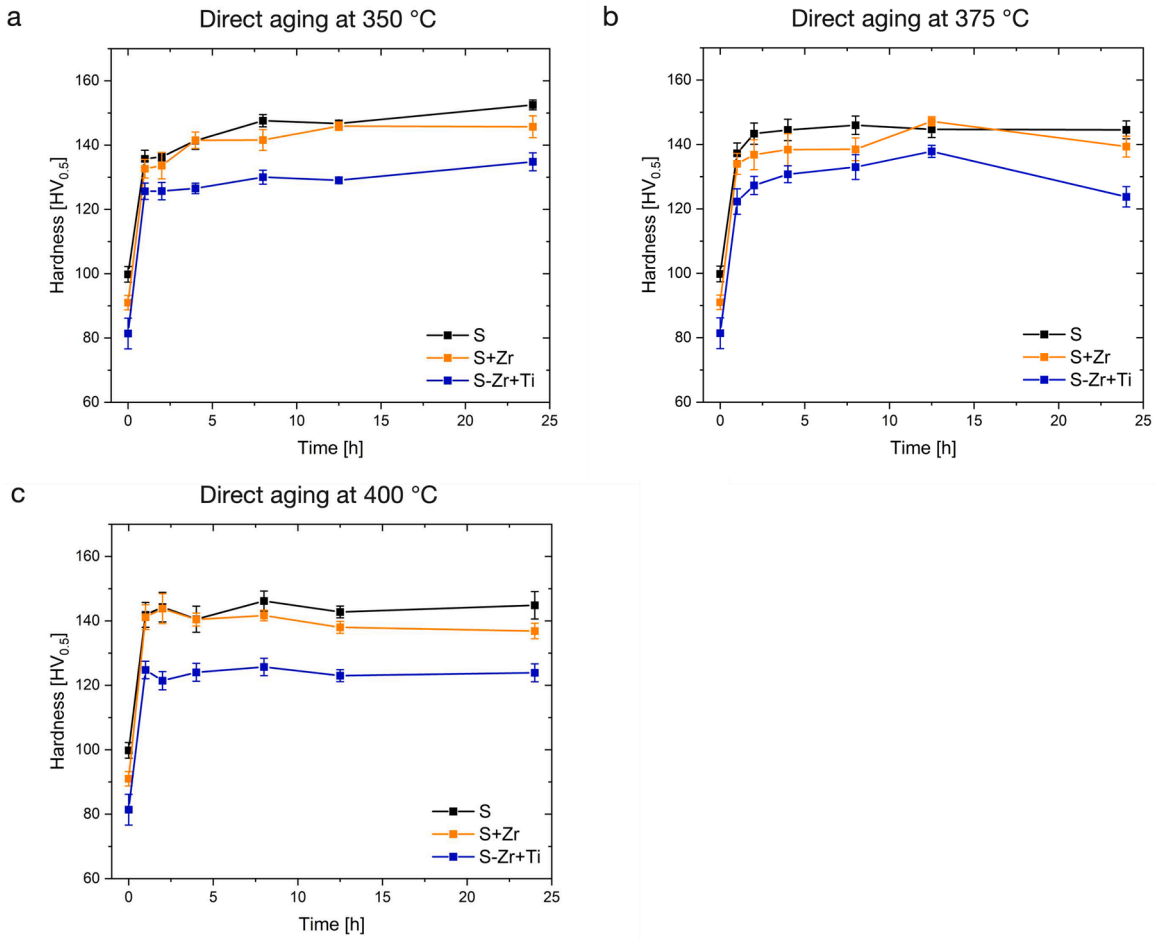

Fig. 7. Aging curves of the S, S+Zr, and S-Zr+Ti alloys collected at 350 °C (a), 375 °C (b) and 400 °C (c).

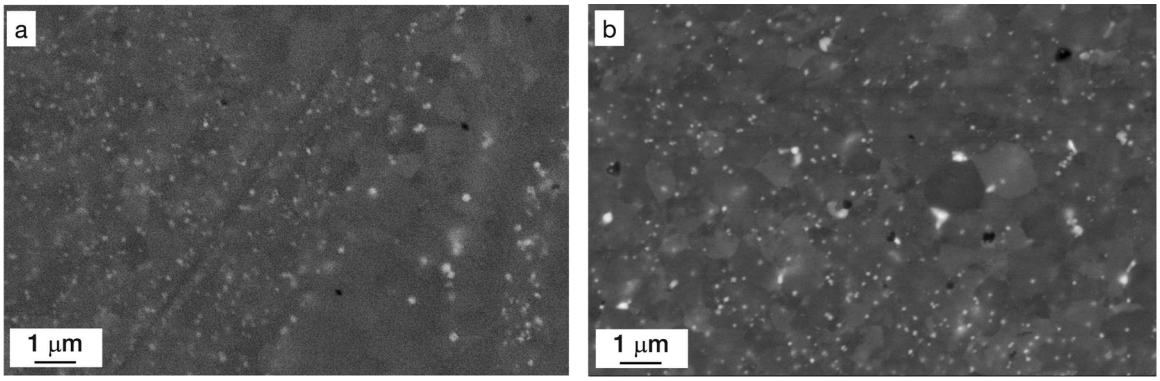

Fig. 8. SEM images of the S alloy in as built (a) and directly aged at 375 °C for 12 h (b).

the overall reduced number of inoculants led to a lower quantity of Al3M secondary precipitates, while the presence of Ti resulted in a sluggish precipitation.

- Direct aging treatments led to significant increases in microhardness, with comparable peak hardness recorded after 12 h at 375 °C of 147.2 HV0.5 for the reference alloy and the Zr-enriched variant, whereas in the alloy containing Zr and Ti, the achieved peak hardness was 137.8 HV0.5.
- Blending different feedstocks to synthesize experimental powders offers a straightforward and cost-effective method for exploring various compositions. Despite residual partially fused high-melting point Zr and Ti powder particles found in the as built microstructure, the effects of induced changes in chemical compositions could be reasonably identified. In the next steps of the investigation, pre-alloyed powders will be atomized to target specific compositions identified from the findings of the current study and more detailed analyses by TEM will be carried out to characterize the aging precipitates.

CRediT authorship contribution statement

F. Larini: Writing – original draft, Investigation. **R. Casati:** Writing – review & editing, Validation, Methodology, Conceptualization. **S. Marola:** Writing – review & editing, Validation, Investigation. **C.**

Andrianopoli: Resources. **P. Bajaj:** Resources. **M. Vedani:** Writing – review & editing, Validation, Methodology, Conceptualization.

Declaration of competing interest

The authors declare that they have no known competing financial interests or personal relationships that could have appeared to influence the work reported in this paper.

Acknowledgements

The research did not receive any specific grant from funding agencies in the public, commercial, or not-for-profit sectors.

References

[1] K.V. Wong, A. Hernandez, A review of additive manufacturing, ISRN Mech. Eng. 2012 (2012) 1–10, https://doi.org/10.5402/2012/208760.
[2] T. DebRoy, H.L. Wei, J.S. Zuback, T. Mukherjee, J.W. Elmer, J.O. Milewski, A. M. Beese, A. Wilson-Heid, A. De, W. Zhang, Additive manufacturing of metallic components – process, structure and properties, Prog. Mater. Sci. 92 (2018) 112–224.
[3] T.M. Pollock, A.J. Clarke, S.S. Babu, Design and tailoring of alloys for additive manufacturing, Metall. Mater. Trans. a Phys. Metall. Mater. Sci. 51 (2020) 6000–6019, https://doi.org/10.1007/s11661-020-06009-3.
[4] F. Larini, R. Casati, S. Marola, M. Vedani, Microstructural evolution of a high-strength Zr-Ti-Modified 2139 aluminum alloy for laser powder bed fusion, Metals 13 (2023), https://doi.org/10.3390/met13050924.
[5] H. Karimialavijeh, M. Ghasri-Khouzani, A. Chakraborty, M. Pröbstle, E. Martin, Direct aging of additively manufactured A20X aluminum alloy, J. Alloys. Compd. 968 (2023), https://doi.org/10.1016/j.jallcom.2023.172071.
[6] A.B. Spierings, K. Dawson, P.J. Uggowitzer, K. Wegener, Influence of SLM scan-speed on microstructure, precipitation of al3sc particles and mechanical properties in Sc- and Zr-modified Al-Mg ALLOYS, Mater. Des. 140 (2018) 134–143, https://doi.org/10.1016/j.matdes.2017.11.053.
[7] J. Schmidt, W. Peukert, Dry powder coating in additive manufacturing, Front. Chem. Eng. 4 (2022).
[8] P. Vieth, M. Voigt, C. Ebbert, B. Milkereit, E. Zhuravlev, B. Yang, O. Keßler, G. Grundmeier, Surface inoculation of aluminium powders for additive manufacturing of Al-7075 alloys, in: Proceedings of the Procedia CIRP, Elsevier B. V., 2020, pp. 17–20. Vol. 94.
[9] S. Heiland, B. Milkereit, K.P. Hoyer, E. Zhuravlev, O. Kessler, M. Schaper, Requirements for processing high-strength Alznmgcu alloys with Pbf-Lb/m to achieve crack-free and dense parts, Materials 14 (2021), https://doi.org/10.3390/ma14237190.
[10] J.P. Brüggemann, L. Risse, G. Kullmer, H.A. Richard, Optimization of the fracture mechanical properties of additively manufactured En AW-7075, in: Proceedings of the Procedia Structural Integrity, Elsevier B.V., 2018, pp. 311–316. Vol. 13.
[11] Al alloys L-PBF elementum 3D material data sheet Available online: https://www.elementum3d.com/data-sheets/ (accessed on 3 April 2023).
[12] R. Konecna, T. Varmus, G. Nicoletto, M. Jambor, Influence of build orientation on surface roughness and fatigue life of the Al2024-RAM2 alloy produced by laser powder bed fusion (L-PBF), Metals 13 (2023), https://doi.org/10.3390/met13091615.
[13] T. Fedotowsky, B. Williams, P.R. Gradl, D.C. Tinker, AL6061-RAM2 development and hot-fire testing using additive manufacturing laser powder directed energy deposition for liquid rocket engine channel-cooled nozzles, in: Proceedings of the AIAA SCITECH 2024 Forum, Reston, Virginia, American Institute of Aeronautics and Astronautics, 2024. January 8.
[14] P.A. Rometsch, Y. Zhu, X. Wu, A. Huang, Review of High-strength aluminium alloys for additive manufacturing by laser powder bed fusion, Mater. Des. (2022) 219.
[15] J.H. Martin, B.D. Yahata, J.M. Hundley, J.A. Mayer, T.A. Schaedler, T.M. Pollock, 3D printing of high-strength aluminium alloys, Nature 549 (2017) 365–369, https://doi.org/10.1038/nature23894.
[16] T. Minasyan, I. Hussainova, Laser powder-bed fusion of ceramic particulate reinforced aluminum alloys: a review, Materials 15 (2022).
[17] F. Belelli, R. Casati, F. Larini, M. Riccio, M. Vedani, Investigation on two Ti–B-reinforced Al alloys for laser powder bed fusion, Mater. Sci. Eng.: A (2021) 808, https://doi.org/10.1016/j.msea.2021.140944.
[18] D. Zhang, A. Prasad, M.J. Bermingham, C.J. Todaro, M.J. Benoit, M.N. Patel, D. Qiu, D.H. StJohn, M. Qian, M.A. Easton, Grain refinement of alloys in fusion-based additive manufacturing processes, Metall. Mater. Trans. A Phys. Metall. Mater. Sci. 51 (2020) 4341–4359, https://doi.org/10.1007/s11661-020-05880-4.
[19] M. Roscher, S. Balachandran, D. Mayweg, E. Jägle, Development of Al-Ti-based alloys for laser powder bed fusion, Addit. Manuf. 47 (2021), https://doi.org/10.1016/j.addma.2021.102315.
[20] F. Belelli, R. Casati, M. Vedani, J. Volpp, Design and characterization of Al–Mg–Si–Zr alloys with improved laser powder bed fusion processability, Metall. Mater. Trans. A Phys. Metall. Mater. Sci. 53 (2022), https://doi.org/10.1007/s11661-021-06531-y.
[21] J.R. Croteau, S. Griffiths, M.D. Rossell, C. Leinenbach, C. Kenel, V. Jansen, D. N. Seidman, D.C. Dunand, N.Q. Vo, Microstructure and mechanical properties of Al-Mg-Zr alloys processed by selective laser melting, Acta Mater. 153 (2018) 35–44, https://doi.org/10.1016/j.actamat.2018.04.053.
[22] Z. Lei, S. Wen, H. Huang, W. Wei, Z.G. Nie, Refinement of aluminum and aluminum alloys by Sc and Zr, Metals (2023) 13.
[23] A.B. Spierings, K. Dawson, K. Kern, F. Palm, K. Wegener, SLM-processed Sc- and Zr-modified Al-Mg alloy: mechanical properties and microstructural effects of heat treatment, Mater. Sci. Eng.: A 701 (2017) 264–273, https://doi.org/10.1016/j.msea.2017.06.089.
[24] D. Schimbäck, P. Mair, M. Bärtl, F. Palm, G. Leichtfried, S. Mayer, P.J. Uggowitzer, S. Pogatscher, Alloy design strategy for microstructural-tailored scandium-modified aluminium alloys for additive manufacturing, Scr. Mater. (2022) 207, https://doi.org/10.1016/j.scriptamat.2021.114277.
[25] F. Belelli, R. Casati, C. Andrianopoli, F. Cuccaro, M. Vedani, Investigation and characterization of an Al-Mg-Zr-Sc alloy with reduced Sc content for laser powder bed fusion, J. Alloys. Compd. (2022) 924, https://doi.org/10.1016/j.jallcom.2022.166519.
[26] Study on the Critical Raw Materials for the EU 2023 – Final Report.
[27] C.M. Cepeda-Jiménez, F. Potenza, E. Magalini, V. Luchin, A. Molinari, M.T. Pérez-Prado, Effect of energy density on the microstructure and texture evolution of Ti-6Al-4V manufactured by laser powder bed fusion, Mater. Charact. (2020) 163, https://doi.org/10.1016/j.matchar.2020.110238.
[28] Q. Chen, K. Wu, G. Sterner, P. Mason, Modeling precipitation kinetics during heat treatment with Calphad-based tools, J. Mater. Eng. Perform. 23 (2014) 4193–4196, https://doi.org/10.1007/s11665-014-1255-6.
[29] A.B. Spierings, K. Dawson, T. Heeling, P.J. Uggowitzer, R. Schäublin, F. Palm, K. Wegener, Microstructural features of Sc- and Zr-modified Al-Mg alloys processed by selective laser melting, Mater. Des. 115 (2017) 52–63, https://doi.org/10.1016/j.matdes.2016.11.040.
[30] S. Griffiths, M.D. Rossell, J. Croteau, N.Q. Vo, D.C. Dunand, C. Leinenbach, Effect of laser rescanning on the grain microstructure of a selective laser melted Al-Mg-Zr Alloy, Mater. Charact. 143 (2018) 34–42, https://doi.org/10.1016/j.matchar.2018.03.033.
[31] H.R. Kotadia, G. Gibbons, A. Das, P.D. Howes, A review of laser powder bed fusion additive manufacturing of aluminium alloys: microstructure and properties, Addit. Manuf. (2021) 46.
[32] K.E. Knipling, D.N. Seidman, D.C. Dunand, Ambient- and high-temperature mechanical properties of isochronally Aged Al-0.06Sc, Al-0.06Zr and Al-0.06Sc-0.06Zr (at.%) alloys, Acta Mater. 59 (2011) 943–954, https://doi.org/10.1016/j.actamat.2010.10.017.
[33] K.E. Knipling, D.C. Dunand, D.N. Seidman, Nucleation and precipitation strengthening in dilute Al-Ti and Al-Zr Alloys, Metall. Mater. Trans. A Phys. Metall. Mater. Sci. 38 (2007) 2552–2563, https://doi.org/10.1007/s11661-007-9283-6.
[34] O.R. Myhr, O. Grong, S.J. Andersen, Modelling of the age hardening behaviour of Al-Mg-Si alloys, Acta Mater. 49 (2001) 65–75, https://doi.org/10.1016/S1359-6454(00)00301-3.
[35] W. Wen, Y. Zhao, J.G. Morris, The effect of mg precipitation on the mechanical properties of 5xxx aluminum alloys, Mater. Sci. Eng.: A 392 (2005) 136–144, https://doi.org/10.1016/j.msea.2004.09.059.